Tellus SERIES A DYNAMIC METEOROLOGY AND OCEANOGRAPHY
PUBLISHED BY THE INTERNATIONAL METEOROLOGICAL INSTITUTE IN STOCKHOLM

Anomalous Arctic surface wind patterns and their impacts on September sea ice minima and trend

By BINGYI WU[1]*, JAMES E. OVERLAND[2] and ROSANNE D'ARRIGO[3], [1]*Chinese Academy of Meteorological Sciences, Beijing, China*; [2]*NOAA/Pacific Marine Environmental Laboratory, Seattle, WA, USA*; [3]*Tree-Ring Laboratory, Lamont-Doherty Earth Observatory, Palisades, NY 10964, USA*

(Manuscript received 23 July 2011; in final form 17 April 2012)

ABSTRACT

We used monthly mean surface wind data from the National Centers for Environmental Prediction/National Centers for Atmospheric Research (NCEP/NCAR) reanalysis dataset during the period 1979–2010 to describe the first two patterns of Arctic surface wind variability by means of the complex vector empirical orthogonal function (CVEOF) analysis. The first two patterns respectively account for 31 and 16% of its total anomalous kinetic energy. The leading pattern consists of the two subpatterns: the northern Laptev Sea (NLS) pattern and the Arctic dipole (AD) pattern. The second pattern contains the northern Kara Sea (NKS) pattern and the central Arctic (CA) pattern. Over the past two decades, the combined dynamical forcing of the first two patterns has contributed to Arctic September sea ice extent (SIE) minima and its declining trend. September SIE minima are mainly associated with the negative phase of the AD pattern and the positive phase of the CA pattern during the summer (July to September) season, and both phases coherently show an anomalous anticyclone over the Arctic Ocean. Wind patterns affect September SIE through their frequency and intensity. The negative trend in September SIE over the past two decades is associated with increased frequency and enhanced intensity of the CA pattern during the melting season from April to September. Thus, it cannot be simply attributed to the AD anomaly characterised by the second empirical orthogonal function mode of sea level pressure north of 70°N. The CA pattern exhibited interdecadal variability in the late 1990s, and an anomalous cyclone prevailed before 1997 and was then replaced by an anomalous anticyclone over the Arctic Ocean that is consistent with the rapid decline trend in September SIE. This paper provides an alternative way to identify the dominant patterns of climate variability and investigate their associated Arctic sea ice variability from a dynamical perspective. Indeed, this study investigates only the role of surface wind dynamical forcing in resulting September SIE minima and trend in terms of CVEOF, without even considering contributions from other factors.

Keywords: Arctic surface wind patterns, Arctic dipole pattern, central Arctic pattern, September sea ice extent minima, trend, interdecadal variability

1. Introduction

September Arctic sea ice extent (SIE) has shown a pronounced negative trend over the past two decades, and frequently reached its previous record lows (Maslanik and Serreze, 1999; Serreze et al., 2003, 2007; Stroeve et al., 2005; Comiso et al., 2008). In September 2007, SIE reached a mere 4.28×10^6 km^2, 23% smaller than the previous record low of 5.56×10^6 km^2 in September 2005 (Stroeve et al., 2008). The key factor for this reduction of Arctic SIE is thinning of sea ice in recent decades (Holloway and Sou, 2002; Lindsay and Zhang, 2005; Maslanik et al., 2007; Stroeve et al., 2008), which may be attributed to the combined effects of increased air temperature, changes in ocean currents and sea-water temperature, radiative flux, wind forcing and ice-albedo feedback (Lindsay and Zhang, 2005; Shimada et al., 2006; Serreze et al., 2007; Steele et al., 2008; Polyakov et al., 2010). Polyakov et al. (2010) showed that the temperature of intermediate-depth Atlantic water has increased during recent decades, and that the Atlantic warm water layer moved closer to the overlying water, leading to decreased Arctic sea ice thickness. Shimada et al. (2006) proposed that increased Pacific Ocean warm water inflow caused sea ice loss in the Arctic Ocean. Thinning of sea ice and ice-albedo positive feedback further favour sea ice melting (Zhang et al., 2008), which, in turn, dominates interannual variability in

*Corresponding author.
email: wby@cams.cma.gov.cn

Citation: Tellus A 2012, **64**, 18590, http://dx.doi.org/10.3402/tellusa.v64i0.18590

Arctic sea ice thickness (Laxon et al., 2003). The dynamic impact of winds on Arctic sea ice has been discussed extensively (Thorndike and Colony, 1982; Proshutinsky and Johnson, 1997; Rigor et al., 2002; Serreze et al., 2003, Spreen et al., 2011; and others). Wind forcing influences spatial distribution of sea ice, sea ice transport out of the Arctic Basin into the northern North Atlantic and summer Pacific warm water inflow into the Arctic Ocean, particularly when there is thinning of sea ice, which allows a more efficient coupling of surface winds and sea ice (Shimada et al., 2006). Previous observations and simulations have also suggested that sea ice thickness variability is controlled partly by wind forcing (Polyakov and Johnson, 2000; Zhang and Hunke, 2001; Holloway and Sou, 2002; Laxon et al., 2003; Stroeve et al., 2011; Spreen et al., 2011). Carmack and Melling (2011) indicated that anomalous wind patterns and albedo feedback played crucial roles in the rapid loss of Arctic sea ice in recent years.

Under the precondition of thinning of the Arctic sea ice, many studies have investigated possible explanations for the observed record lows in September SIE. Serreze et al. (2003) discussed persistence of summer cyclone activity and its impact on sea ice divergence and rapid melt. Some studies attributed the record low of SIE in September 2007 to the combined effect of thinning of sea ice during recent decades and an anticyclonic pattern over the Arctic Ocean (Stroeve et al., 2008; Lindsay et al., 2009). Zhang et al. (2008) indicated that anomalous winds and ice-albedo feedback are the main reasons for the summer sea ice anomaly of 2007. Perovich et al. (2008) suggested that solar heating and ice-albedo feedback contributed to summer sea ice retreat in 2007. Wang et al. (2009) addressed the role of the Arctic dipole (AD) anomaly in triggering the record lows of September SIE, and suggested that the atmospheric pattern produced a strong meridional wind anomaly that drove more sea ice out of the Arctic Ocean into the northern North Atlantic during the summers of 1995, 1999, 2002, 2005 and 2007. On the other hand, Overland and Wang (2010) evaluated the persistence and seasonality of the Arctic Oscillation (AO) and AD anomaly, and argued that reduction of sea ice has a direct connection to increased atmospheric 1000–500 hPa thickness fields, but not necessarily to sea level pressure (SLP).

Although a number of studies have emphasised the roles of wind forcing on resulting September SIE minima, important scientific issues remain. For example, one issue is the need to characterise the dominant patterns of summer Arctic surface wind variability that are closely associated with Arctic September SIE. This issue is crucial for understanding the mechanisms for September sea ice minima and its negative trend from a dynamical perspective. Another question is whether September sea ice minima are directly associated with a particular anomalous wind pattern. Wu and Johnson (2010a) did not address these questions, although they revealed dominant patterns of Arctic winter (October to March of the following year) monthly mean surface wind variability. In addition, this study differs from that of Ogi et al. (2010), as they stressed the analysis of 925 hPa anomalous wind patterns derived from a linear regression on differences in Arctic September SIE. Thus, Ogi et al. (2010) did not identify dominant patterns of summer surface wind variability.

The motivation of the present study is to explore dominant patterns of Arctic summer surface wind variability and their association with September SIE minima and its trend. It should be emphasised that we focus exclusively on the role of dynamical wind forcing in resulting September SIE record lows and its trend, without considering the potential roles of any other factors. In order to reveal trends of Arctic surface wind variability, we use the area-weighted year-round data to extract dominant wind patterns, unlike the study of Wu and Johnson (2010a). Our results indicate that the negative trend in September SIE over the past two decades is mainly associated with increased frequency and enhanced intensity of the second wind pattern during the melting season from April to September, and cannot be simply attributed to the AD anomaly characterised by the second empirical orthogonal function mode of SLP north of 70°N.

2. Data and methods

The data used in the present study include (1) monthly mean SLP and surface wind fields (10 m above the ground) for the period 1979–2010 obtained from the NCEP/NCAR reanalysis I, (2) the monthly mean Arctic sea ice concentration (SIC) dataset (on a 1° latitude × 1° longitude grid) for the period 1979–2010 obtained from the British Atmospheric Data Centre (BADC, http://badc.nerc.ac.uk/data/hadisst/).

We chose the latitude band of 70°N–90°N as our study domain, consistent with the previous analyses of Johnson et al. (1999) and Wu et al. (2006a). This study constructs a complex Hermitian matrix based on area-weighted monthly surface wind anomalies to extract dominant statistical patterns of Arctic surface wind variability from 1979 to 2010, for a total of 384 months. We use year-round data to determine frequencies and trends of anomalous patterns of surface wind variability. This study then analyses wind patterns in the summer (July to September) season, during which cumulative effects of surface wind variability contribute to September SIE. The vector analysis method used in this study is the same as that used elsewhere (e.g. Kundu and Allen, 1976; Brink and Muench, 1986; Kaihatu et al., 1998; Wu et al., 2006b, 2008; Wu and Johnson, 2010a, 2010b), also known as complex vector empirical orthogonal function (CVEOF) analysis.

See Appendix for further information about the statistical and physical details of the CVEOF method.

This CVEOF method has clear advantages over the empirical orthogonal function (EOF) method for identifying dominant patterns of climate variability and their associated Arctic sea ice anomalies from a dynamical perspective. Here we use surface winds and SLP data to compare differences derived from the two methods. Each wind pattern derived from the CVEOF essentially reflects an anomalous kinetic energy associated with a specific spatial variability in anomalous wind fields (see Appendix). In contrast, an SLP pattern derived from EOF reflects a variance contribution to SLP variability. An SLP pattern derived from EOF has only positive and negative polarities, with no complex spatial evolution, whereas a wind pattern derived from the CVEOF does. Wu and Johnson (2010a) showed that the leading surface wind pattern north of 70°N consists of two different subpatterns, and corresponding SLP anomalies exhibit distinctive spatial structures that clearly differ from the AO or the central Arctic (CA) pattern characterised by the leading SLP pattern north of 70°N. Consequently, SLP and wind patterns, respectively, derived from EOF and the CVEOF are not interchangeable in characterizing climate variability. In addition, sea ice conditions are sensitive to slight shifts in the position of high- and low-pressure centres that are not characterised by EOF patterns (Stroeve et al., 2011). Thus, we consider the CVEOF method to be superior to EOF from a purely dynamical perspective for characterizing the variety and complexity of climate variability.

3. Dominant spatial features of surface wind variability

The leading pattern (leading CVEOF) of monthly mean surface wind variability (for a total of 384 months) accounts for 31% of the variance (or the total anomalous kinetic energy). This value is lower than that determined when considering only the winter months: Wu and Johnson (2010a) found that the leading winter wind pattern accounts for 35.3% of the variance. Figure 1 shows the time series of the leading phase, and the real and imaginary parts of the leading complex principal component. No apparent trend is observed in these time series. To investigate the leading pattern's spatial evolution, composite analyses were performed for the following typical four different leading phase ranges: '0°' phase ($\theta < 45°$ or $\theta \geq 315°$), '90°' phase ($135° > \theta \geq 45°$), '180°' phase ($225° > \theta \geq 135°$) and '270°' phase ($315° > \theta \geq 225°$). The composite analyses were carried out using only the summer (July to September) monthly mean anomalous wind fields (for a total of 96 summer months). Table 1 shows their frequencies for the typical four different phase ranges.

For the '0°' phase, an anomalous cyclonic surface wind covers the entire Arctic Basin and its Eurasian marginal seas, with its centre near the north of the Laptev Sea. Southerly and southwesterly anomalies originating from the Pacific sector penetrate the Arctic Ocean, then becoming northwesterly anomalies occupying the Barents-Kara Seas (Fig. 2a). Correspondingly, negative SLP anomalies cover most of the Arctic Ocean and from the Barents Sea eastwards to the East Siberian Sea, and there is an anomalous centre over the northern Laptev Sea (Fig. 2e). When the leading wind pattern is in its '90°' phase, there is a pair of anomalous anticyclonic and cyclonic surface winds over the Barents-Kara Seas and close to the Beaufort Sea, and anomalous southerly and southeasterly covers the northern Greenland Sea and the western Barents Sea (Fig. 2b). The spatial distribution of corresponding SLP anomalies shows a dipole structure (Fig. 2f), which is dynamically consistent with the anomalous wind pattern in Fig. 2b. The anomalous wind and SLP patterns corresponding to the '180°' ('270°') phase show the opposite scenario to that in the '0°' ('90°') phase (Fig. 2c, d, g and h). The '270°' phase of the leading wind pattern has the largest frequency (26 times), and the second largest is its '180°' phase (25 times) (Table 1).

Figure 2 shows that the leading wind pattern consists of the two subpatterns, and corresponding SLP anomalies also display different spatial structures. Consequently, the leading phase reflects the spatial evolution of the two subpatterns and their frequencies. In this study, the two subpatterns are termed the northern Laptev Sea (NLS) pattern and the AD pattern, respectively. The regression maps of summer monthly mean surface winds, regressed on the real and imaginary parts of the leading complex principal component, respectively, resemble Fig. 2a and b (not shown). Consequently, the real and imaginary parts can be regarded as two intensity indices to characterise the NLS and AD patterns, respectively. Thus, the NLS pattern incorporates the '0°' and '180°' phases of the leading wind pattern, and a positive (negative) phase of the NLS pattern corresponds to the '0°' ('180°') phase. Similarly, the AD pattern incorporates the '90°' and '270°' phases of the leading wind pattern, and a positive (negative) phase of the AD pattern corresponds to the '90°' ('270°') phase. Fig. 2a and b, respectively, resembles Fig. 7a and b of Wu and Johnson (2010a) where surface wind anomalies are derived from a linear regression on winter months (October to March) during the period 1979–1998. Regression maps of summer monthly mean SLP, regressed on the real and imaginary parts of the leading complex principal component, closely resemble Fig. 2e and f, respectively (not shown).

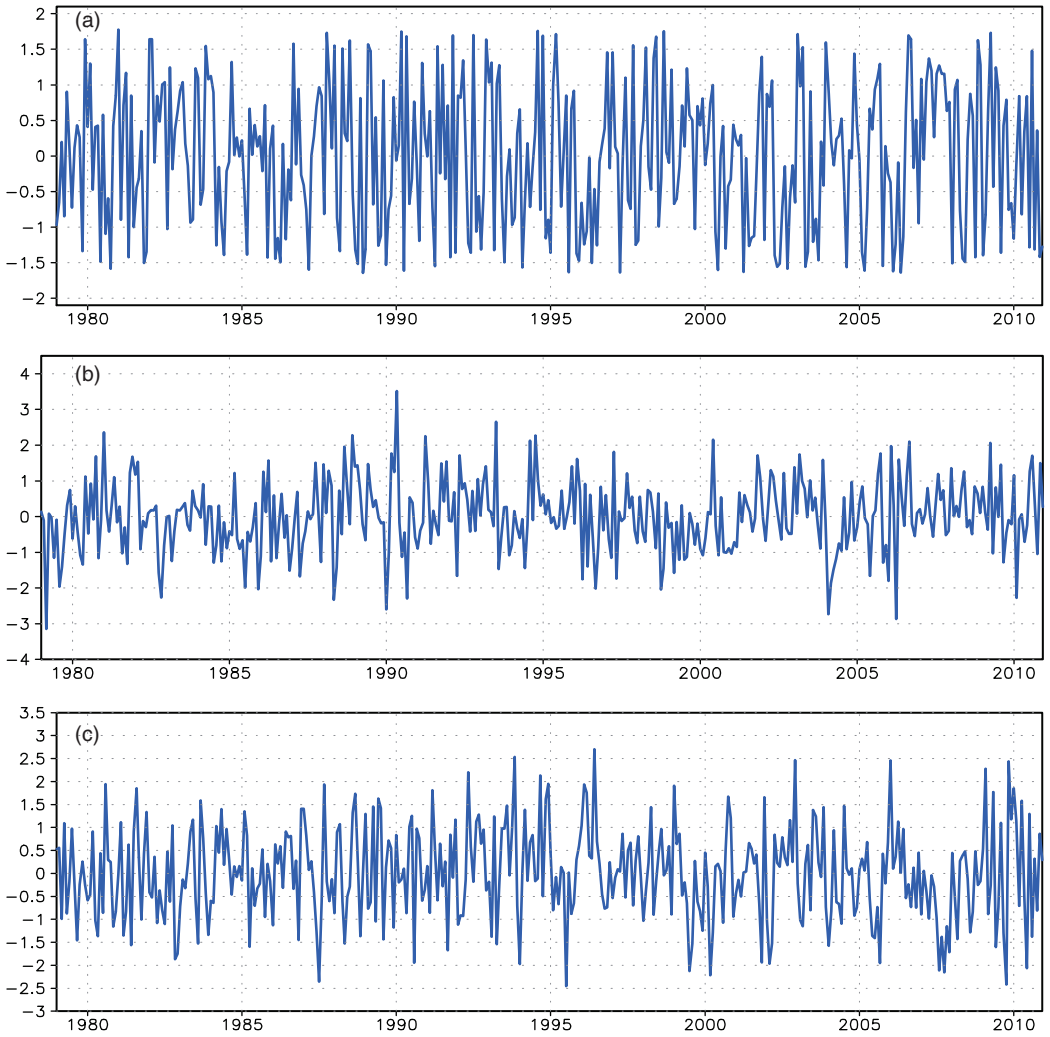

Fig. 1. Normalised monthly mean time series of (a) the leading phase, (b) real and (c) imaginary parts of the leading complex principal component, and three time series are obtained from deviations from their means divided by their *SDs* from 1979 to 2010 (for a total of 384 months).

Similar analyses are applied to the second wind pattern of monthly mean surface wind variability (second CVEOF), which accounts for 16% of the variance. For the '0°' phase of the second wind pattern, there is an anomalous cyclone over the Arctic Ocean and its marginal seas (Fig. 3a). There are two points that make this pattern different from that of Fig. 2a. One is its centre over the north of the Barents-Kara Seas rather than a position north of the Laptev Sea, and the other is southwesterly anomalies covering the northeastern North Atlantic and Norwegian Sea. The spatial distribution of SLP anomalies resembles that in Fig. 2e, but is further shifted to the North Atlantic sector (Fig. 3e). When the second wind pattern is in its '90°' phase, an anomalous anticyclone with its centre close to the CA Ocean replaces the anomalous cyclone in its '0°' phase, and coherent northerly anomalies appear over the area from the Greenland Sea to the Barents Sea (Fig. 3b). Over the Barents-Kara Seas, there are cyclonic wind anomalies, which differ from the summer surface wind anomalies in Ogi et al. (2010; their Fig. 1). Correspondingly, the anomalous SLP forms a dipole structure with opposing anomalous centres, respectively, over the

Table 1. Frequencies for different phase ranges in the summer months (July to September) from 1979 to 2010

Phase	Leading wind pattern	Second wind pattern
'0°'	21	18
'90°'	24	31
'180°'	25	17
'270°'	26	30

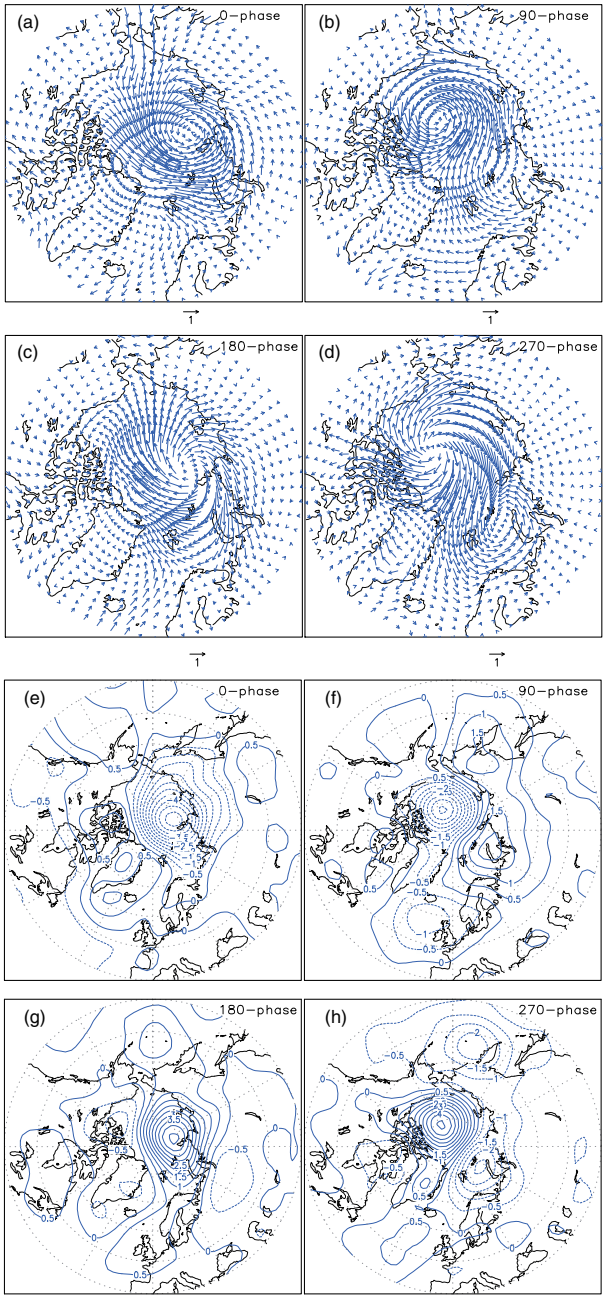

Fig. 2. (a) Composite of summer monthly mean surface wind anomalies for the '0°'($\theta < 45°$ or $\theta \geq 315°$) phase of the leading surface wind pattern, (b)–(d) as in (a) but for the '90°'($135° > \theta \geq 45°$), '180°'($225° > \theta \geq 135°$), '270°'($315° > \theta \geq 225°$) phases, respectively; (e)–(h) as in (a)–(d) but for corresponding SLP anomalies; units: m s^{-1} in (a)–(d); hPa in (e)–(h).

Arctic Ocean and northern Asian continent close to Taymyr (Fig. 3f). The anomalous wind and SLP patterns in the '180°' and '270°' phases also, respectively, exhibit the opposite scenario to that in the '0°' and '90°' phases (Fig. 3c, d, g and h). Frequencies for the '90°' and '270°' phases of the second wind pattern, respectively, are 31 and 30 times greater than for the '0°' and '180°' phases (Table 1), implying that the wind patterns in Fig. 3b and d are more frequent during the study period. The second wind pattern also contains the two subpatterns, and they are named as the northern Kara Sea (NKS) pattern and the CA pattern, respectively.

Further analysis confirms that the real and imaginary parts of the second complex principal component can be regarded as two intensity indices to depict the NKS and CA patterns, respectively. Thus, the NKS (CA) pattern incorporates the '0°' ('90°') and '180°' ('270°') phases of the second wind pattern.

4. Physical significance of the observed phase evolution of wind patterns

It is seen that from the '0°' to '270°' phases negative centres in SLP anomalies exhibit a counterclockwise rotation evolution over the Arctic Ocean and its marginal seas (Fig. 2e–h). A very similar evolution also emerges in 500 hPa anomalous geopotential heights, and geopotential height and SLP anomalies show the quasi-barotropic structure (Fig. 4a–d). This phenomenon essentially reflects a counterclockwise migration process of the central position of the polar vortex in the mid-low troposphere, as shown in Fig. 4e and f. For the '0°' and '180°' phases of the leading wind pattern, central positions of the polar vortex are situated, respectively, over the Eurasian and North American regions of the Arctic Ocean, and the '90°' and '270°' phases, respectively, correspond to central positions of the polar vortex being close to the Beaufort Sea and Nordic Sea regions of the Arctic Ocean. Consequently, the leading wind pattern physically reflects dominant features of the spatial evolution in the central position of the polar vortex. Additionally, the shape, extent and intensity of the polar vortex all impact on the wind pattern, although this is beyond the scope of this paper.

Although the phase evolution of the second wind pattern is also associated with the spatial shift of the polar vortex, the central position of the polar vortex does not display an apparent clockwise or counterclockwise rotation over the Arctic Ocean (Fig. 4g and h). The '0°' phase of the second wind pattern corresponds to the central position of the polar vortex over the CA Ocean close to the northern Barents Sea (Fig. 4g). Then it further migrates towards to northern Asia continent in its '90°' phase (Fig. 4h). From the '90°' to '180°' phases, the central position of the polar vortex shifts from the Asian to the North American regions of the Arctic Ocean. Finally, it moves to the CA Ocean close to the Beaufort Sea in its '270°' phase.

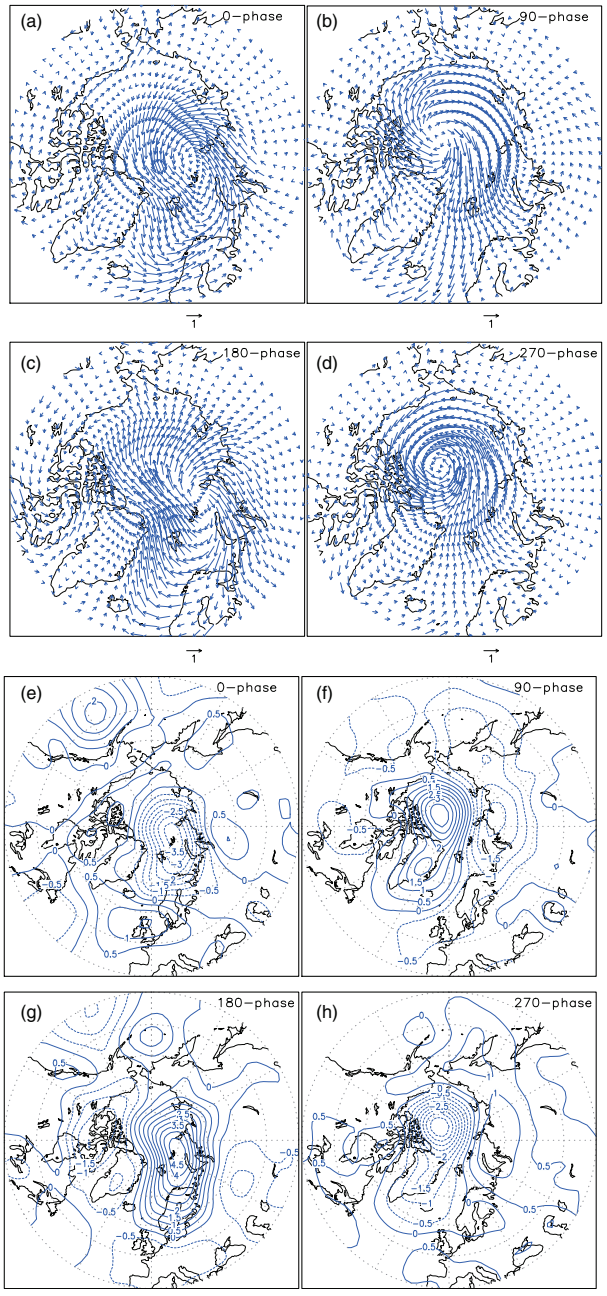

Fig. 3. As in Fig. 2, but for the second wind pattern.

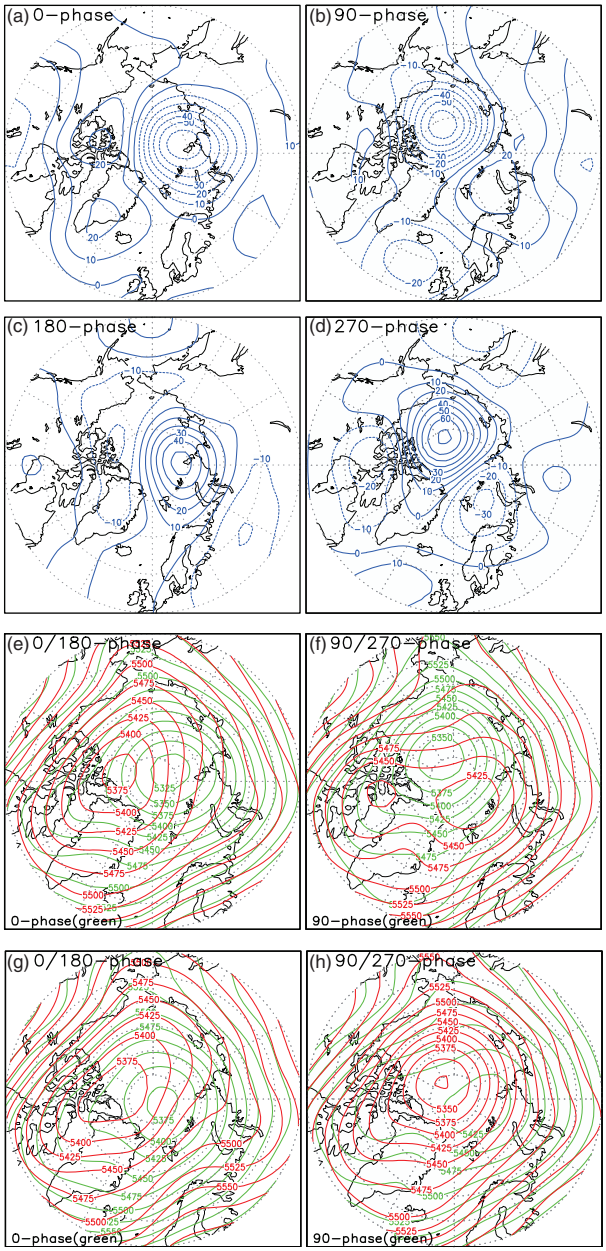

Fig. 4. (a) Composite of summer monthly mean 500 hPa height anomalies for the '0°'($\theta < 45°$ or $\theta \geq 315°$) phase of the leading wind pattern, (b)–(d) as in (a) but for the '90°'($135° > \theta \geq 45°$), '180°'($225° > \theta \geq 135°$), '270°'($315° > \theta \geq 225°$) phases, respectively; (e) composite of summer monthly mean 500 hPa heights for the '0°' (green contour) and '180°' (red contour) phases, (f) same as in (e), but for the '90°' (green contour) and '270°' (red contour) phases, (g) and (h), respectively, same as in (e) and (f), but for the second wind pattern, contour intervals are 10 in (a)–(d) and 25 gpm in (e)–(h), respectively.

5. Impacts of summer surface wind patterns on September SIE

In Section 3, we indicated that the real and imaginary parts of the first two complex principal components can be regarded as indices that characterise wind patterns associated with different phases. Time series of their summer (July to September) means are shown in Fig. 5. Although the NLS pattern displays a trend that is significant at the 95% level (Fig. 5a), it does not significantly correlate with September SIE (Fig. 5e). The AD pattern exhibits a negative trend but it is not significant (Fig. 5b), whereas the CA pattern shows a positive trend at the 99% significance

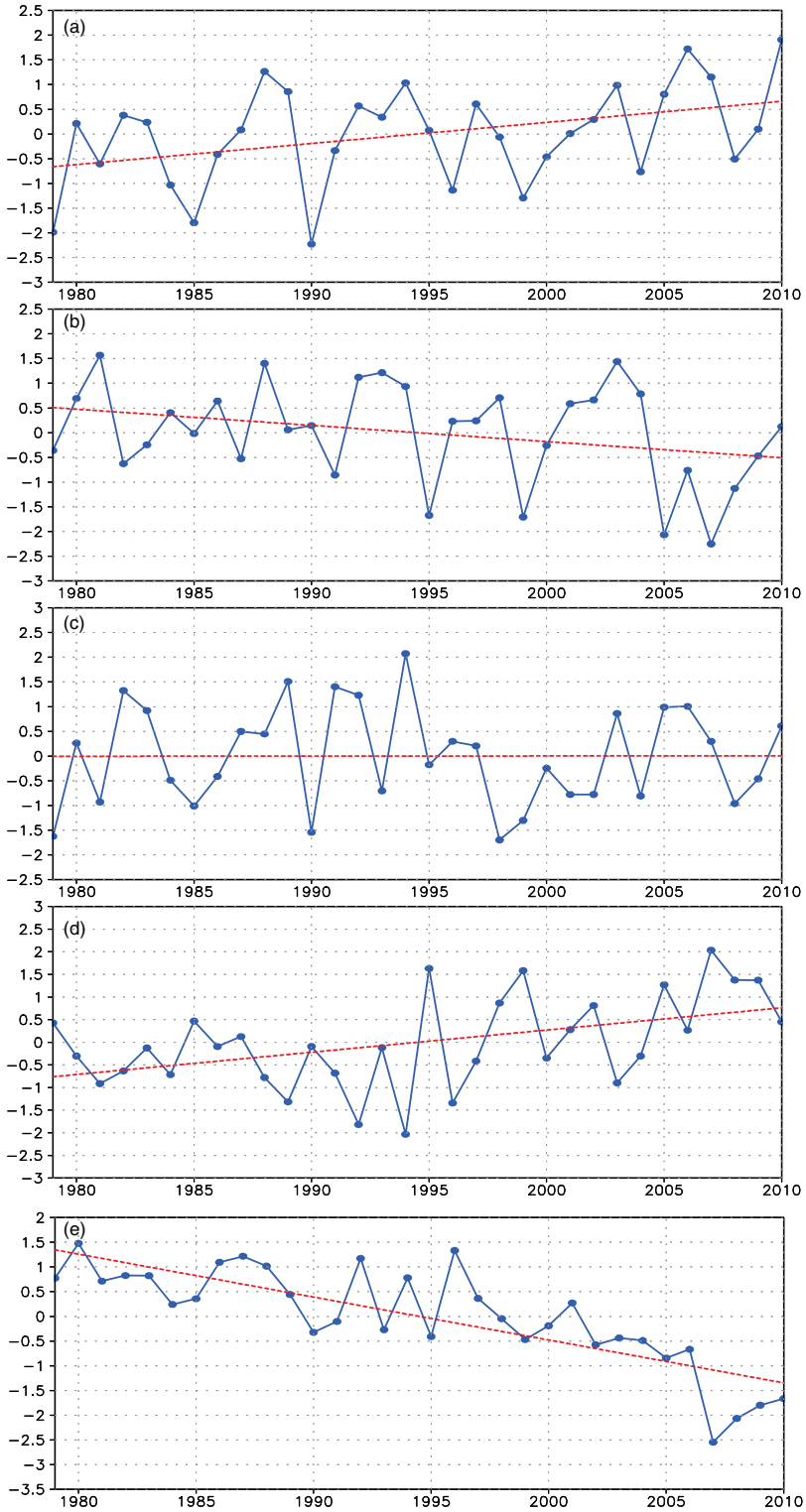

Fig. 5. Normalised time series of (a) the NLS and (b) AD patterns, respectively, derived from summer (July to September) means of the real and imaginary parts of the leading complex principal component, (c) and (d), respectively, as in (a) and (b), but for the NKS and CA patterns, derived from the second complex principal component, (e) normalised time series of Arctic September SIE (SIC $> 15\%$), derived from BADC SIC data, red-dashed lines represent their trends, five time series are obtained from deviations from their means divided by their *SDs*.

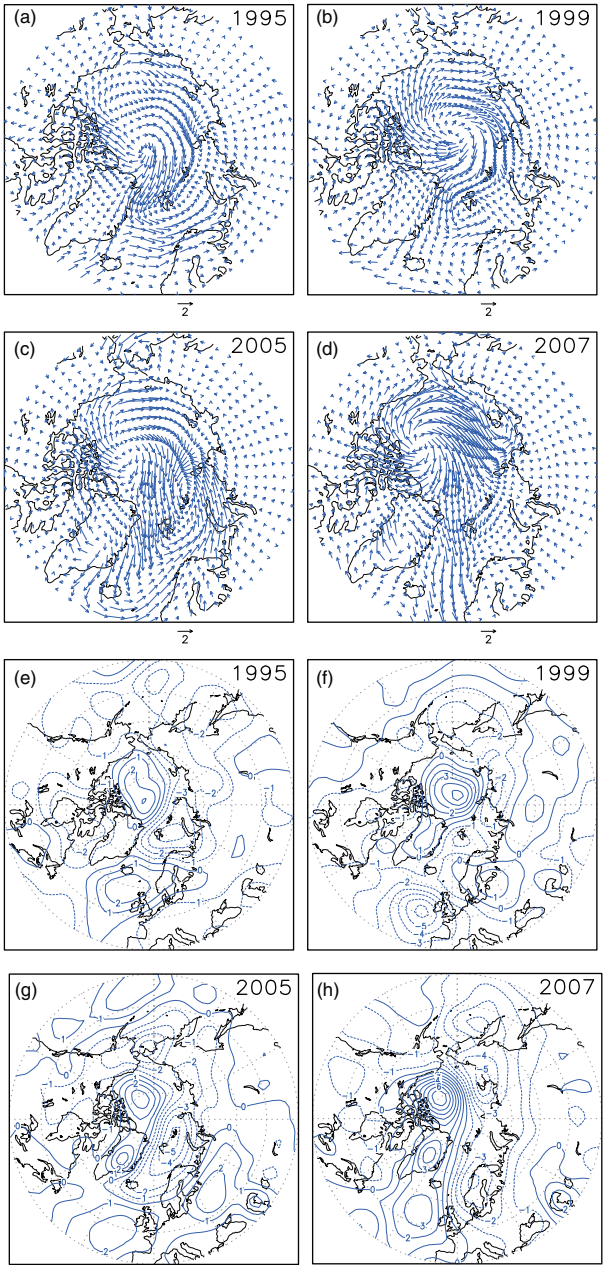

Fig. 6. Summer (July to September) mean surface wind anomalies in (a) 1995, (b) 1999, (c) 2005, (d) 2007, (e)–(h) as in (a)–(d), respectively, but for summer mean SLP anomalies; units: $m\,s^{-1}$ in (a)–(d) and hPa in (e)–(h).

level (Fig. 5d). September SIE is significantly correlated with the AD and CA patterns (Fig. 5b and d) after removing their linear trends (their correlations are 0.46 and -0.61, at the 99% significance level, and their raw correlations are 0.50 and -0.68, respectively).

Among the four surface wind patterns, only the negative phase of the AD pattern (Fig. 5b) and the positive phase of the CA pattern (Fig. 5d) correspond well to September SIE minima in 1995, 1999, 2005 and 2007 (Fig. 5e). Composite analyses of surface wind and SLP anomalies also support this point (see Fig. 2d, h and 3b, f) that anomalous meridional winds favour the Transpolar Drift Stream that drives sea ice out of the Arctic Ocean into the Greenland–Barents Seas. Observations have shown that there was more sea ice transport out of the Arctic Ocean through the Fram Strait in the summers of 2005 and 2007 (Kwok, 2009), consistent with our results herein.

Although the AD and CA patterns contributed to September SIE minima in 1995, 1999, 2005 and 2007, this does not imply that their contributions are equal, as shown in Fig. 6. In the summers of 1995, 1999, 2005 and 2007, a common feature was an anomalous anticyclone occupying the Arctic Ocean. Main centres of cyclonic wind anomalies were located, respectively, over the northern Barents Sea in 1995 (Fig. 6a), between the Greenland Sea and the Barents Sea in 1999 (Fig. 6b), the NKS in 2005 (Fig. 6c) and the Laptev Sea in 2007 (Fig. 6d). In 2007, a weak anomalous cyclonic centre was visible over the Barents Sea, unlike that shown in Fig. 3b. Thus, anomalous surface wind patterns in these summers showed a great similarity to a negative phase of the AD pattern (Fig. 2d), indicating that the AD pattern is more linked to September SIE minima relative to the CA pattern. An comparison of the intensity between these two wind patterns also supports this point (except for in 1995); the intensity of the AD (CA) pattern was 22.89 (23.19) in 1995, 23.36 (22.45) in 1999, 28.23 (18.01) in 2005 and 30.81 (28.86) in 2007 (note that the intensity of wind patterns is non-dimensional). Since the intensity of the two wind patterns was comparable in 1995, the leading wind pattern was more important relative to the second. Indeed, a weak anomalous cyclonic centre over the Barents Sea and a strong anomalous cyclonic centre over the Laptev Sea in 2007 reflected an enhanced impact of the CA pattern. In 1995, 1999 and 2005, summer mean SLP anomalies closely resemble that in Fig. 2h (Fig. 6e–g). In 2007, there were two negative centres between the Laptev and East Siberian Seas and Scandinavia, respectively (Fig. 6h), reflecting the combined effect of two wind patterns (Fig. 2h and 3f).

The negative phase of the AD pattern and the positive phase of the CA pattern have frequently appeared and contributed to recent September SIE minima, as shown in Fig. 7a and b. The negative phase of the AD pattern has frequently emerged in three summer months: 2 (1995), 2 (1999), 3 (2005) and 3 (2007) times. The NLS and AD patterns, however, do not exhibit any trend in its cumulative frequencies during the melting season from April to September (not shown). In summers of 1995, 1999, 2002 and from 2004 to 2010, the positive phase of the CA pattern occurred at least twice each summer, and in the summer of 2007 it persisted for three summer months.

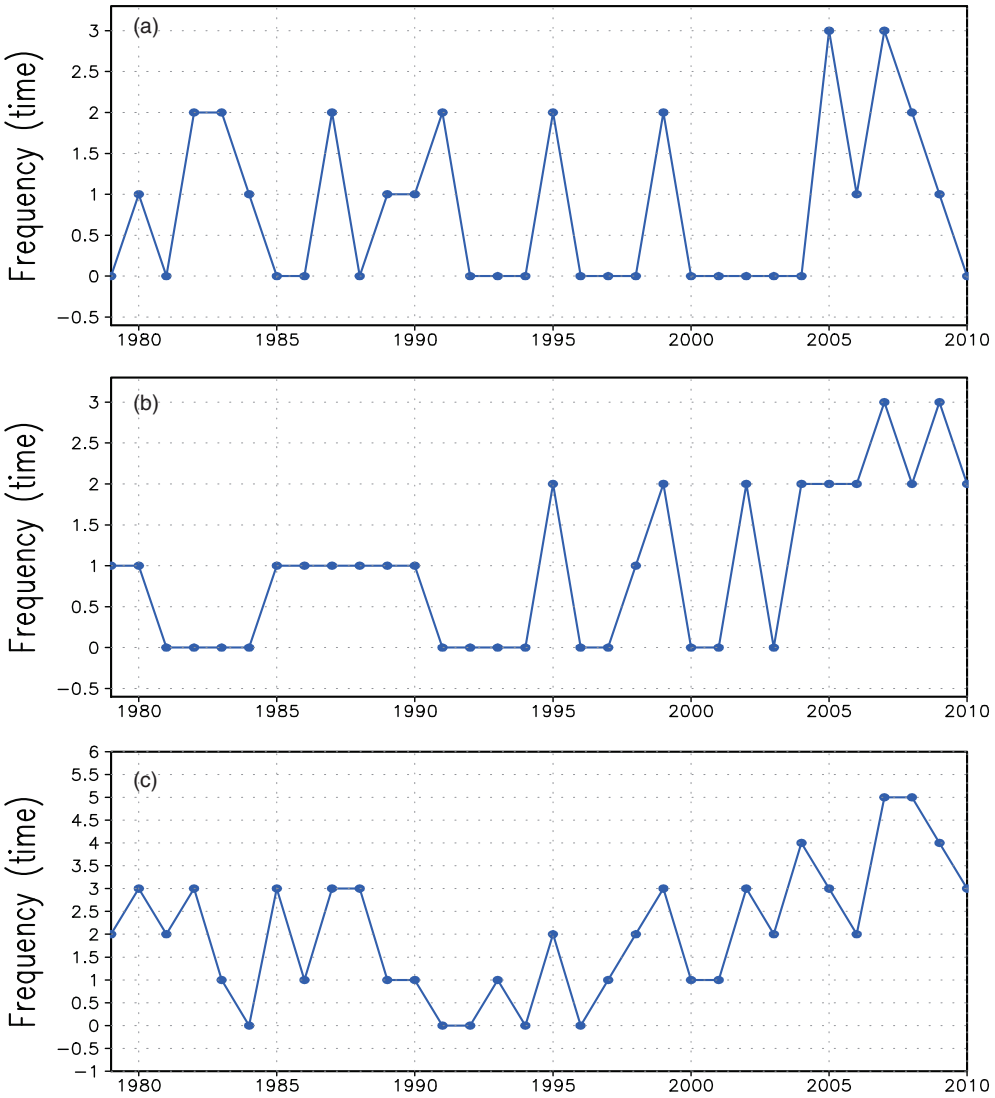

Fig. 7. (a) Frequencies of the negative phase of the AD pattern from July to September, (b) as in (a), but for the positive phase of the CA pattern, (c) cumulative frequencies of the positive phase of the CA pattern in the melting season from April to September.

In addition, there is an apparent positive trend since the early 1990 in its cumulative frequencies from April to September (Fig. 7c).

The impacts of both the negative phase of the AD pattern and the positive phase of the CA pattern (Fig. 2d and 3b) on September SICs are shown in Fig. 8. Significant negative SIC anomalies emerge in the area close to the Eurasian marginal seas, with positive SIC anomalies in the vicinity of the Fram Strait (Fig. 8a). A positive phase of the CA pattern (Fig. 3b) is associated with negative trends in September SICs, particularly in the Pacific sector of the Arctic Ocean and the Eurasian marginal seas (Fig. 8b and c). Although SIC anomalies shown in Fig. 8a and d exhibit a similar spatial structure, the magnitude of anomalies shown in Fig. 8d is weaker relative to those shown in Fig. 8a. On one hand, the two anomalous wind patterns shown in Fig. 2d and 3b favour sea ice transport out of the Arctic Ocean and Eurasian marginal seas into the Greenland–Barents Seas, which contributes directly to open water production because the absence of freezing replenishes open water areas (Kwok, 2009). On the other hand, the two anomalous anticyclones over the Arctic Ocean (Fig. 2d and 3b) may favour sea ice convergence to the CA Ocean via Ekman transport at the surface. Consequently, increased frequency from April to September and enhanced intensity of the CA pattern have contributed to the observed negative trend in September SIE (Fig. 7c and 5d). Ogi et al. (2010) also investigated the influence of summer (June to September) mean surface wind (925 hPa) anomalies on summer Arctic SIE through a linear regression on the

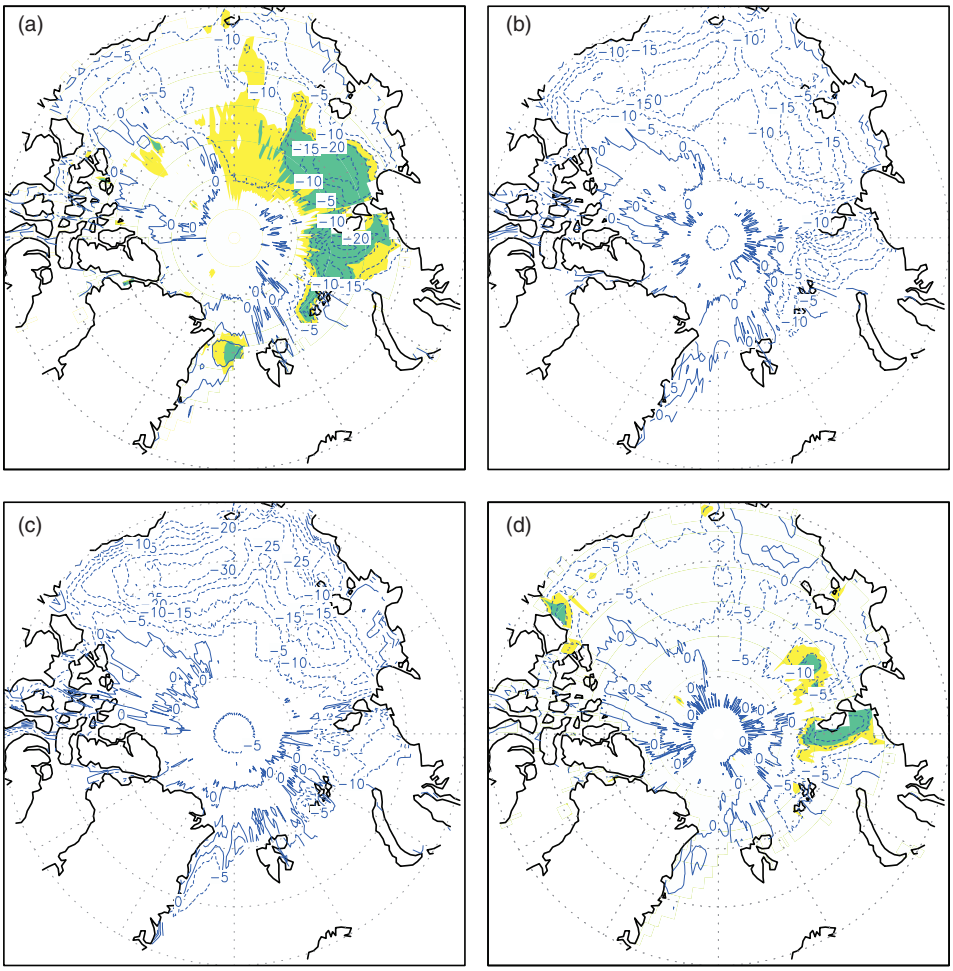

Fig. 8. (a) September SIC anomalies derived from a linear regression on the converted normalised time series of the AD pattern, (b) as in (a) but for regressed on the normalised time series of the CA pattern, (c) as in (b) but for regressed on the trend in the CA pattern, (d) as in (c) but for regressed on the detrended time series of the CA pattern, colour-shading areas denote SIC anomalies exceeding the 95 and 99% significance levels, respectively.

inverted one-year difference of September Arctic SIE ($-\Delta$SIE) time series. Although summer surface wind anomalies in their study are very similar to those in Fig. 3b over the Arctic Ocean, differences between them are also apparent over the Barents–Kara Seas (i.e. their surface wind anomalies did not exhibit cyclonic anomalies over the Barents–Kara Seas, see their Fig. 1).

6. Associations with SLP patterns

To explore the relationships between wind and SLP patterns that derive from EOF analysis, EOF analysis was applied to monthly mean SLP north of 70°N from 1979 to 2010. The first three EOFs respectively account for 59, 13 and 9% of the variance. Here, we focus on the summer season averaged over July to September. The AD pattern is significantly correlated with EOF3 ($r = 0.91$) (Fig. 9a). Although the regression maps of summer mean SLP, respectively, regressed on the AD pattern and EOF3 are very similar to each other (Fig. 9b and c), their time evolutions show visible differences in 2005 and 2007. In fact, the effect of the SLP pattern (EOF3) on Fram Strait sea ice flux is important, although it accounts for only 9.1% of the variance of SLP variability (Wu and Johnson, 2007). The spatial distribution of summer mean SLP anomalies associated with the CA pattern also differs from the AD anomaly characterised by EOF2, as shown in Fig. 10. In addition to apparent differences in their time evolutions (their correlation is 0.52, after removing their trends the correlation is 0.36) (Fig. 10a), differences in SLP anomalies are distinct. For the CA pattern, corresponding SLP anomalies show

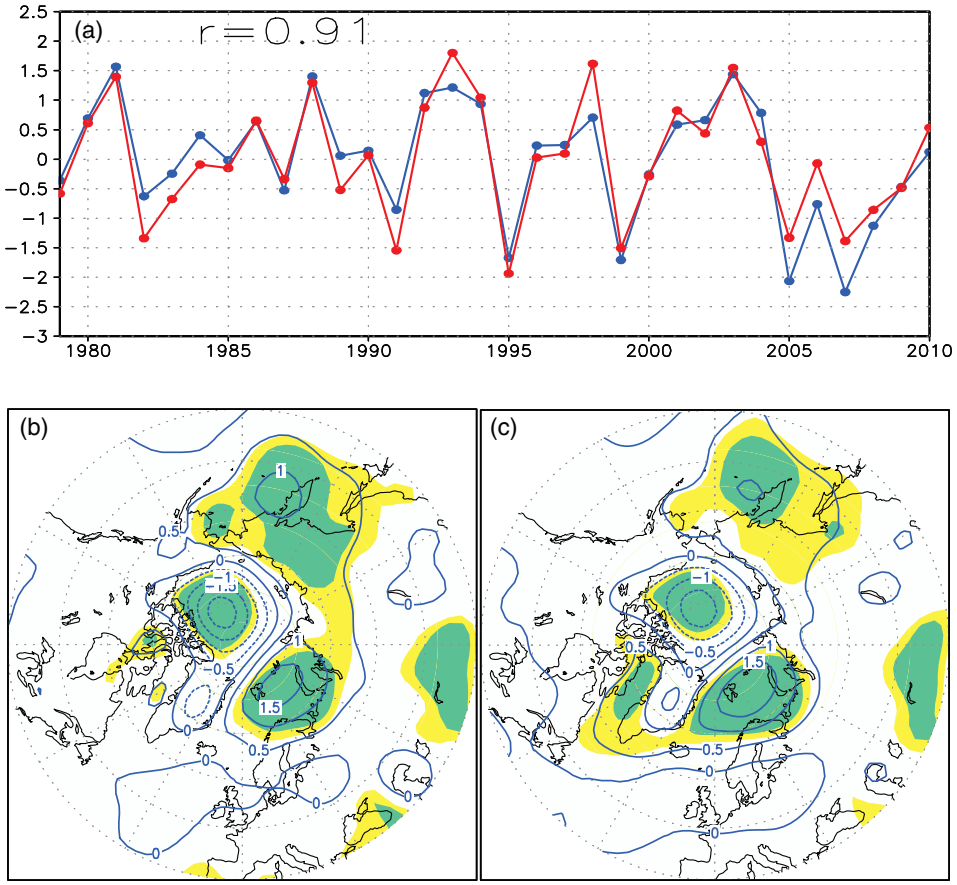

Fig. 9. (a) Normalised time series of the AD pattern (blue line) and EOF3 (red line), their correlation is 0.91, both time series are obtained from deviations from their means divided by their *SDs*, (b) and (c) regression maps of summer mean SLP, regressed on the AD pattern and EOF3, respectively, colour-shading areas denote SLP anomalies exceeding the 95 and 99% significance levels, respectively.

a monopole structure over the CA Ocean with negative SLP anomalies over the Eurasian marginal seas and northern Eurasia (Fig. 10d). For the summer AD anomaly, the opposing anomalous centres are located over the Canadian Archipelago and adjacent ocean area and between the Laptev and Kara Seas, respectively (Fig. 10e). In fact, the AD anomaly (or EOF2) is significantly correlated with the NLS pattern: their correlation is 0.77 (the correlation is 0.72 after removing their trends), consistent with the result of Wu and Johnson (2010a). However, the summer SLP regression map, regressed on the time series in Fig. 5a, closely resembles Fig. 2e (not shown), differing from Fig. 10e.

7. Conclusion and discussion

Using the CVEOF method, this study shows the first two patterns of Arctic month mean surface wind variability and their linkages with September SIE from 1979 to 2010. The first two patterns account for 31 and 16% of the total anomalous kinetic energy, respectively. The spatial evolution of the first two patterns, along with corresponding SLP and 500 hPa geopotential height anomalies for the four different typical phase ranges (‘0°’, ‘90°’, ‘180°’ and ‘270°’), was investigated using data averaged over the summer months. It is found that the spatial evolution of the leading wind pattern for the four different typical phase ranges essentially reflects a counterclockwise migration process of the central position of the polar vortex in the mid–low troposphere. Although the phase evolution of the second wind pattern is also associated with the spatial shift of the polar vortex, the central position of the polar vortex does not display an apparent clockwise or counterclockwise rotation over the Arctic Ocean. The leading wind pattern consists of the two subpatterns: the NLS and AD patterns. Similarly, the second wind pattern contains the NKS and CA patterns.

Arctic September SIE minima are linked to the negative phase of the AD pattern and the positive phase of the CA pattern, and wind patterns drive September SIE minima through their frequency and intensity. Over the past two decades, increased frequency and

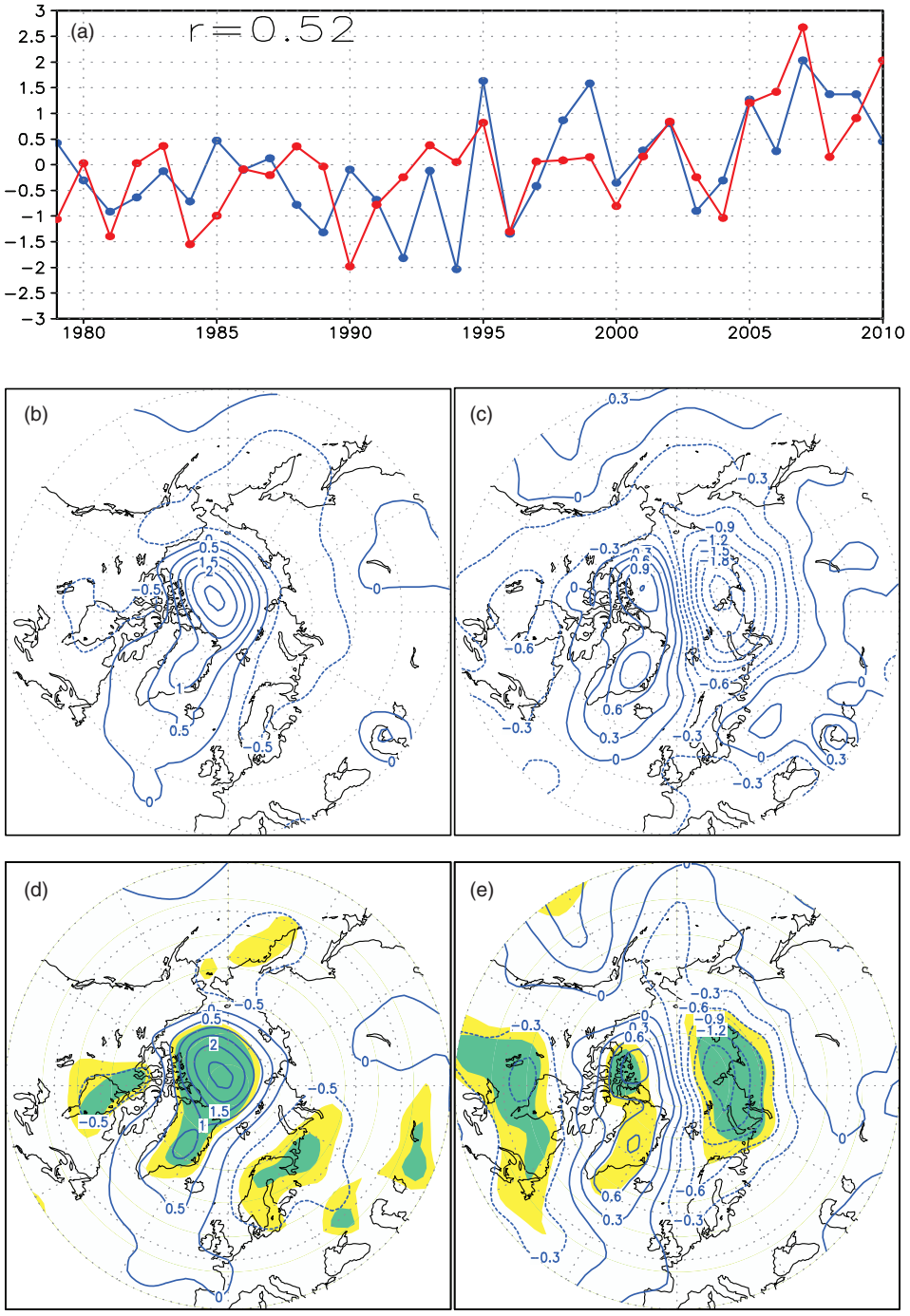

Fig. 10. (a) Normalised time series of the CA pattern (blue line) and EOF2 (red line), their correlation is 0.52 (the correlation becomes 0.36 after removing their trends), both time series are obtained from deviations from their means divided by their *SDs*, (b) and (c) regression maps of summer mean SLP, regressed on the CA pattern and EOF2, respectively, (d) and (e) as in (b) and (c), respectively, but for regressed on their detrended time series, colour-shading areas denote SLP anomalies exceeding the 95 and 99% significance levels, respectively.

strengthened intensity of the CA pattern have contributed substantially to the observed negative trend in September SIE.

A further analysis indicates that the cumulative deviation time series of the CA pattern (Fig. 5d) reached its lowest value in 1997 (-8.75), implying that this year may

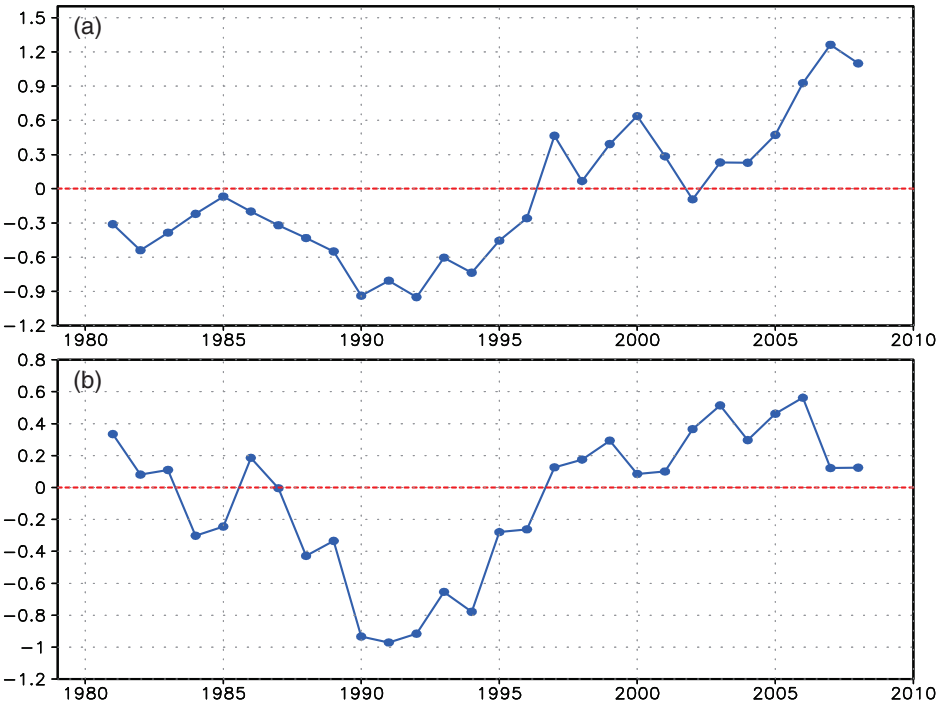

Fig. 11. (a) Five-year running means of the normalised time series of the CA pattern, (b) as in (a) but for spring (April to June) mean, two normalised time series are obtained from deviations from their means divided by their *SDs*.

be a turning point of abrupt change. A cumulative deviation time series can be written as:

$$y(t) = \sum_{i=1}^{t} [x(i) - \bar{x}], \quad t = 1, 2, \ldots, N, \; \bar{x} = \frac{1}{N} \sum_{t=1}^{N} x(t),$$

and it can be applied to estimate possible key turning points in the time series of $x(t)$ (Bell, 1980; Dugmore et al., 2007). The moving t-test method is also used to the time series of the CA pattern, and the analysis result further confirms that '1997' is a turning point at the 95% significance level. A five-year running mean of the time series of the CA pattern shows an apparent positive trend since 1990. Negative phases prevailed before 1997, followed by dominant positive phases (Fig. 11a), which correspond well to the rapidly declining trend in September SIE (Fig. 5e). The positive trend in Fig. 11a is consistent with increases in frequency of the CA pattern (Fig. 7c). A similar phenomenon was observed in the spring (April to June) season, as shown in Fig. 11b. In contrast, other wind patterns in this study, EOF2 and EOF3 of SLP variability north of 70°N, do not display this phenomenon.

A similar interdecadal variability was also detected in the calculated atmospheric vorticity index over the CA Ocean to the north of the Laptev Sea, where the vorticity index showed a negative trend after 1990 and became negative after 1996 (see Fig. 2b of Polyakov and Johnson, 2000), which is dynamically consistent with our results. Consequently, the interdecadal (or multidecadal) variability of the Arctic atmospheric circulation may be an important contributing factor to the short-term trends in wind pattern. This hypothesis is supported by several studies (Polyakov and Johnson, 2000; Polyakov et al., 2004). Polyakove et al. (2004) suggested that Atlantic water temperature, Arctic surface air temperature, SIE and fast ice thickness in the Siberian marginal seas exhibit coherent low-frequency oscillations (LFO) on the time scales of 50–80 yrs, and that the short-term trends are strongly amplified by the LFO. This may imply that recovery of September SIE probably is possible in the future if we only consider the role of surface wind patterns. It should be stressed again, as we have noted, that herein we have focused exclusively on the role of surface wind forcing in resulting September SIE minima and its trend in terms of CVEOF method, without considering contributions from other factors.

8. Acknowledgements

The authors thank three anonymous reviewers for support and constructive criticism, which helped significantly to improve this paper. This study was supported by GYHY200906017, State Oceanic Administration Project

(201205007), the National Natural Science Foundation of China (40875052), the Project of Chinese Academy of Meteorological Sciences (2010Z003) and the Program of China Polar Environment Investigation and Assessment (2011–2015).

9. Appendix

A.1. Statistical and physical meanings of the CVEOF method

A.1.1. Analytical analysis Through an analysis of a simple complex Hermitian matrix, we explain statistical and physical meanings of a resolution of the CVEOF method. We use $U_{ij} = u_{ij} + iv_{ij}$ to construct a complex Hermitian matrix (i, spatial position; j, time; u_{ij} and v_{ij} denote wind anomalies, units are m s^{-1}), and only select two spatial positions and two observations:

$$\overline{U}_{ij} = u_{ij} - iv_{ij}$$

$$U = \begin{bmatrix} U_{11} & U_{12} \\ U_{21} & U_{22} \end{bmatrix}, \quad U^* = \begin{bmatrix} \overline{U}_{11} & \overline{U}_{21} \\ \overline{U}_{12} & \overline{U}_{22} \end{bmatrix},$$

U^* is the conjugate transpose of U.

The complex Hermitian matrix is:

$$C = \frac{1}{2} UU^* = \frac{1}{2} \begin{bmatrix} U_{11}\overline{U}_{11} + U_{12}\overline{U}_{12} & U_{11}\overline{U}_{21} + U_{12}\overline{U}_{22} \\ U_{21}\overline{U}_{11} + U_{22}\overline{U}_{12} & U_{21}\overline{U}_{21} + U_{22}\overline{U}_{22} \end{bmatrix}$$

where:

$$\begin{aligned} U_{11}\overline{U}_{21} + U_{12}\overline{U}_{22} &= (u_{11}u_{21} + v_{11}v_{21} + u_{12}u_{22} + v_{12}v_{22}) \\ &\quad + i(u_{21}v_{11} + u_{22}v_{12} - u_{11}v_{21} - u_{12}v_{22}) \\ U_{21}\overline{U}_{11} + U_{22}\overline{U}_{12} &= (u_{21}u_{11} + v_{21}v_{11} + u_{22}u_{12} + v_{22}v_{12}) \\ &\quad - i(u_{21}v_{11} + u_{22}v_{12} - u_{11}v_{21} - u_{12}v_{22}) \\ U_{11}\overline{U}_{11} + U_{12}\overline{U}_{12} &= u_{11}^2 + v_{11}^2 + u_{12}^2 + v_{12}^2 \\ U_{21}\overline{U}_{21} + U_{22}\overline{U}_{22} &= u_{21}^2 + v_{21}^2 + u_{22}^2 + v_{22}^2 \end{aligned}$$

Here, let:

$$A = \frac{u_{11}^2 + v_{11}^2 + u_{12}^2 + v_{12}^2}{2} = \frac{\sum_{j=1}^{2} u_{1j}^2 + \sum_{j=1}^{2} v_{1j}^2}{2}$$

$$B = \frac{u_{21}^2 + v_{21}^2 + u_{22}^2 + v_{22}^2}{2} = \frac{\sum_{j=1}^{2} u_{2j}^2 + \sum_{j=1}^{2} v_{2j}^2}{2}$$

$$\begin{aligned} C0 &= \frac{u_{11}u_{21} + v_{11}v_{21} + u_{12}u_{22} + v_{12}v_{22}}{2} \\ &= \frac{\sum_{j=1}^{2} u_{1j}u_{2j} + \sum_{j=1}^{2} v_{1j}v_{2j}}{2} \end{aligned}$$

$$\begin{aligned} D0 &= \frac{u_{21}v_{11} + u_{22}v_{12} - u_{11}v_{21} - u_{12}v_{22}}{2} \\ &= \frac{\sum_{j=1}^{2} u_{2j}v_{1j} - \sum_{j=1}^{2} u_{1j}v_{2j}}{2} \end{aligned}$$

Thus:

$$C = \begin{bmatrix} A & C0 + iD0 \\ C0 - iD0 & B \end{bmatrix}$$

Two eigenvalues of the complex Hermitian matrix are:

$$\lambda_1 = \frac{(A+B) + \sqrt{(A-B)^2 + 4(C0^2 + D0^2)}}{2}$$

$$\lambda_2 = \frac{(A+B) - \sqrt{(A-B)^2 + 4(C0^2 + D0^2)}}{2}$$

For the leading CVEOF:

$$CX = \lambda_1 X,$$

where $X = \begin{bmatrix} X_1 \\ X_2 \end{bmatrix}$ is the leading complex eigenvector:

$$\begin{aligned} &(A - \lambda_1)X_1 + (C0 + iD0)X_2 = 0.0 \\ &(C0 - iD0)X_1 + (B - \lambda_1)X_2 = 0.0 \\ &\text{Let } X_1 = \mathrm{XR}_1 + i\mathrm{XI}_1 = 1.0 + i0.0, \end{aligned}$$

Thus:

$$\begin{aligned} X_2 &= \mathrm{XR}_2 + i\mathrm{XI}_2 \\ &= \frac{\lambda_1 - A}{(C0 + iD0)} = \frac{(\lambda_1 - A)C0}{(C0^2 + D0^2)} - i\frac{(\lambda_1 - A)D0}{(C0^2 + D0^2)} \end{aligned}$$

Consequently, XR_2 and XI_2 are non-dimensional quantities, that is, complex eigenvectors are non-dimensional quantities.

The leading complex principal component is:

$$\begin{aligned} \mathrm{PC}_{11} &= \mathrm{TR}_{11} + i\mathrm{TI}_{11} \\ &= (u_{11}\mathrm{XR}_1 + u_{21}\mathrm{XR}_2 - v_{11}\mathrm{XI}_1 - v_{21}\mathrm{XI}_2) \\ &\quad + i(u_{11}\mathrm{XI}_1 + u_{21}\mathrm{XI}_2 + v_{11}\mathrm{XR}_1 + v_{21}\mathrm{XR}_2) \end{aligned}$$

and

$$\begin{aligned} \mathrm{PC}_{12} &= \mathrm{TR}_{12} + i\mathrm{TI}_{12} \\ &= (u_{12}\mathrm{XR}_1 + u_{22}\mathrm{XR}_2 - v_{12}\mathrm{XI}_1 - v_{22}\mathrm{XI}_2) \\ &\quad + i(u_{12}\mathrm{XI}_1 + u_{22}\mathrm{XI}_2 + v_{12}\mathrm{XR}_1 + v_{22}\mathrm{XR}_2) \end{aligned}$$

Thus, the real and imaginary parts of the leading complex principal component are dimensional quantities (units are m s^{-1}).

The leading phase is:

$$\theta(j) = \arctan\left[\frac{\mathrm{TI}_{1j}}{\mathrm{TR}_{1j}}\right].$$

A.1.2. Statistical and physical meaning A and B, respectively, represent the sum of variance of u and v at two different spatial positions. $C0$ is the sum of co-variance. $D0$ is the difference of co-variances. Consequently, the real and imaginary parts of the leading eigenvector have statistical meaning.

In fact, the CVEOF method itself divides anomalous wind fields into a series of orthogonal wind patterns that are ranked in order of magnitude of the variance contribution or anomalous kinetic energy. The leading wind pattern has the maximum variance contribution or anomalous kinetic energy, measured by λ_1 (units are $m^2 s^{-2}$). For the above case:

$$\lambda_1 + \lambda_2 = \frac{u_{11}^2 + v_{11}^2 + u_{12}^2 + v_{12}^2 + u_{21}^2 + v_{21}^2 + u_{22}^2 + v_{22}^2}{2},$$

reflecting the total anomalous kinetic energy. Thus, each wind pattern corresponds to an anomalous kinetic energy of specific spatial variability in anomalous wind fields.

Since XR_2 and XI_2 are non-dimensional quantities, the real and imaginary parts of the leading complex eigenvector have no apparent physical meaning. In contrast, the real and imaginary parts of the leading complex principal component have physical meaning, reflecting the evolution of specific spatial variability in anomalous wind fields, and they are characterised by the sum of all u and v with different 'weighted' coefficients at a specific time. Those 'weighted' coefficients have statistical meaning. Additionally, the real and imaginary parts of the leading complex principal component are related to each other.

In fact, each pattern of wind field variability extracted from the method consists of two subpatterns (they are either similar or different from each other) that are characterised by the real and imaginary parts of its complex principal component. That is, they determine amplitude (or intensity) and positive/negative polarities of two subpatterns. Additionally, its phase, derived from a ratio of the real and imaginary parts of the complex principal component, determines the spatial evolution status and frequencies of the two subpatterns.

References

Bell, B. 1980. Analysis of viticultural data by cumulative deviations. *J. Interdis. Hist.* **10**, 851–858.

Brink, K. and Muench, R. 1986. Circulation in the point conception-Santa Barbara channel region. *J. Geophys. Res.* **91**(C1), 877–895.

Comiso, J., Parkinson, C., Gersten, R. and Stock, L. 2008. Accelerated decline in the Arctic sea ice cover. *Geophys. Res. Lett.* **35**, L01703. DOI: 10.1029/2007GL031972.

Carmack, E. and Melling, H. 2011. Warmth from the deep. *Nat. Geosci.* **4**, 7–8.

Dugmore, A., Borthwick, D., Church, M., Dawson, A., Edwards, K. and co-authors. 2007. The role of climate in settlement and landscape change in the North Atlantic Islands: an assessment of cumulative deviations in high-resolution proxy climate records. *Hum. Ecol.* **35**, 169–178. DOI: 10.1007/s10745-006-9051-z.

Holloway, G. and Sou, T. 2002. Has Arctic sea ice rapidly thinned? *J. Clim.* **15**, 1691–1701.

Johnson, M., Proshutinsky, A. and Polyakov, I. 1999. Atmospheric patterns forcing two regimes of Arctic ice-ocean circulation: a return to anticyclonic conditions? *Geophys. Res. Lett.* **26**(11), 1621–1624.

Kaihatu, J., Handler, R., Marmorino, G. and Shay, L. 1998. Empirical orthogonal function analysis of ocean surface current using complex and real-vector methods. *J. Atmos. Ocean. Technol.* **15**, 927–941.

Kundu, P. and Allen, J. 1976. Some three-dimensional characteristics of low-frequency current fluctuations near the Oregon Coast. *J. Phys. Oceanogr.* **6**, 181–199.

Kwok, R. 2009. Outflow of Arctic Ocean sea ice into the Greenland and Barents Seas: 1979–2007. *J. Clim.* **22**, 2438–2457. DOI: 10.1175/2008JCLI2819.1.

Laxon, S., Peacock, N. and Smith, D. 2003. High interannual variability of sea ice thickness in the Arctic region. *Nature* **425**, 947–950.

Lindsay, R. and Zhang, J. 2005. The thinning of Arctic sea ice, 1988–2003: how we passed a tipping point? *J. Clim.* **18**, 4879–4894.

Lindsay, R., Zhang, J., Schweiger, A., Steele, M. and Htern, H. 2009. Arctic sea ice retreat in 2007 following thinning trend. *J. Clim.* **22**, 165–176. DOI: 10.1175/2008JCLI2521.

Maslanik, J. and Serreze, M. 1999. On the record reduction in 1998 western Arctic sea-ice cover. *Geophys. Res. Lett.* **26**(13), 1905–1908.

Maslanik, J., Fowler, C., Stroeve, J., Drobot, S., Zwally, J. and co-authors. 2007. A younger, thinner, arctic ice cover: increased potential for rapid, extensive sea-ice loss. *Geophys. Res. Lett.* **34**, L24501. DOI: 10.1029/2007GL032043.

Ogi, M., Yamazaki, K. and Wallace, J. 2010. Influence of winter and summer surface wind anomalies on summer Arctic sea ice extent. *Geophys. Res. Lett.* **37**, L07701. DOI: 10.1029/2009GL042356.

Overland, J. and Wang, M. 2010. Large-scale atmospheric circulation changes are associated with the recent loss of Arctic sea ice. *Tellus* **62A**, 1–9.

Perovich, D., Richter-Menge, J., Jones, K. and Light, B. 2008. Sunlight, water, and ice: extreme Arctic sea ice melt during the summer of 2007. *Geophys. Res. Lett.* **35**, L11501. DOI: 10.1029/2008GL034007.

Polyakov, I., Timokhov, L., Alexeev, V., Bacon, S., Dmitrenko, I. and co-authors. 2010. Arctic Ocean warming contributes to reduced polar ice cap. *J. Phys. Oceanogr.* **40**, 2743–2756.

Polyakov, I. and Johnson, M. 2000. Arctic decadal and interdecadal variability. *Geophys. Res. Lett.* **27**(24), 4097–4100.

Polyakov, I., Alekseev, G., Timokhov, L., Bhatt, U., Colony, R. and co-authors. 2004. Variability of the intermediate Atlantic water of the Arctic Ocean over the last 100 years. *J. Clim.* **17**(23), 4485–4497.

Proshutinsky, A. and Johnson, M. 1997. Two circulation regimes of the wind-driven Arctic Ocean. *J. Geophys. Res.* **102**(C6), 12493–12514.

Rigor, I., Wallace, J. and Colony, R. 2002. Response of sea ice to the Arctic Oscillation. *J. Clim.* **15**, 2648–2663.

Serreze, M., Holland M. and Stroeve, J. 2007. Perspectives on the Arctic's shrinking sea-ice cover. *Science* **315**, 1533–1536. DOI: 10.1126/science, 1139426.

Serreze, M., Maslanik, J., Scambos, T., Fetterer, F., Stroeve, J. and co-authors. 2003. A record minimum arctic sea ice extent and area in 2002. *Geophys. Res. Lett.* **30**(3), 1110. DOI: 10.1029/2002GL016406.

Shimada, K., Kamoshida, T., Itoh, M., Nishino, S., Carmack, E. and co-authors. 2006. Pacific Ocean inflow: influence on catastrophic reduction of sea ice cover in the Arctic Ocean. *Geophys. Res. Lett.* **33**, L08605. DOI: 10.1029/2005GL025624.

Spreen, G., Kwok, R. and Menemenlis, D. 2011. Trend in Arctic sea ice drift and role of wind forcing: 1992–2009. *Geophys. Res. Lett.* **38**, L19501. DOI: 10.1029/2011GL048970.

Steele, M., Ermold, W. and Zhang, J. 2008. Arctic ocean surface warming trends over the past 100 years. *Geophys. Res. Lett.* **35**, L02614. DOI: 10.1029/2007GL031651.

Stroeve, J., Serreze, M., Fetterer, F., Arbetter, T., Meier, W. and co-authors. 2005. Tracking the Arctic's shrinking ice cover: another extreme September minimum in 2004. *Geophys. Res. Lett.* **32**, L04501. DOI: 10.1029/2004GL021810.

Stroeve, J., Serreze, M., Drobot, S., Gearheard, S., Holland, M. and co-authors. 2008. Arctic sea ice extent plummets in 2007. *EOS* **89**(2), 8.

Stroeve, J., Maslanik, J., Serreze, M., Rigor, I., Meier, W. and co-authors. 2011. Sea ice response to an extreme negative phase of the Arctic Oscillation during winter 2009/2010. *Geophys. Res. Lett.* **38**, L02502. DOI: 10.1029/2010GL045662.

Thorndike, A. S. and Colony, R. 1982. Sea ice motion in response to geostrophic winds. *J. Geophys. Res.* **87**(C8), 5845–5852.

Wang, J., Zhang, J., Watanabe, E., Ikeda, M., Mizobata, K. and co-authors. 2009. Is the dipole anomaly a major driver to record lows in Arctic summer sea ice extent? *Geophys. Res. Lett.* **36**, L05706. DOI: 10.1029/2008GL036706.

Wu, B., Wang, J. and Walsh, J. 2006a. Dipole anomaly in the winter arctic atmosphere and its association with sea ice motion. *J. Clim.* **19**, 210–225.

Wu, B., Zhang, R. and D'Arrigo, R. 2006b. Distinct modes of the East Asian winter monsoon. *Mon. Weather Rev.* **134**, 2165–2179.

Wu, B., Zhang, R., Ding, Y. and D'Arrigo, R. 2008. Distinct modes of the East Asian summer monsoon. *J Clim.* **21**, 1122–1138.

Wu, B. and Johnson, M. 2007. A seesaw structure in SLP anomalies between the Beaufort Sea and the Barents Sea. *Geophys. Res. Lett.* **34**, L05811. DOI: 10.1029/2006GL028333.

Wu, B. and Johnson, M. 2010a. Distinct modes of winter arctic sea ice motion and their associations with surface wind variability. *Adv. Atmos. Sci.* **27**(2), 211–229.

Wu, B. and Johnson, M. 2010b. Predominant modes of winter surface wind variability over the Gulf of Alaska. *Int. J. Climatol.* **30**, 256–266.

Zhang, J., Lindsay, R., Strrle, M. and Schweiger, A. 2008. What drove the dramatic retreat of arctic sea ice during summer 2007? *Geophys. Res. Lett.* **35**, L11505. DOI: 10.1029/2008GL034005.

Zhang, Y. and Hunke, E. 2001. Recent Arctic change simulated with a coupled ice-ocean model. *J. Geophys. Res.* **106**, 4369–4390.